

Femtosecond Many-Body Dynamics of Caging: Experiment and Simulation of I₂ Photodissociation—Recombination in Solid Ar

Z. Li, R. Zadoyan, V. A. Apkarian,* and C. C. Martens*

Department of Chemistry, University of California, Irvine, California 92717-2025

Received: October 20, 1994; In Final Form: February 10, 1995[⊗]

The many-body dynamics resulting from I₂ photodissociation in solid Ar are investigated using a combination of time-resolved pump–probe measurements and molecular dynamics simulations. The wavelength dependence of the signals, measured with a time resolution of 120–150 fs, are reported. Polarization experiments indicate that, for the duration of observation, the photodissociation–recombination proceeds adiabatically. Molecular dynamics simulations, combined with the classical Franck principle, are employed to calculate simulated signals, which agree well with experiment. The microscopic dynamics of the system are then investigated by examining individual trajectory data in detail, giving an atomic-scale view of the photoinduced dissociation of I₂ on the A excited electronic surface, the subsequent caging of the photofragments by the lattice, I₂ recombination, and coherent vibrational dynamics of the nascent diatomic molecule. Recombination is found to be a dynamically complex process, involving bidirectional energy flow between molecule and lattice during the early time motion of the photofragments in the solvent cage. The recombination event, when defined as the permanent deexcitation of the I₂ below its dissociation threshold, is not directly associated with any prominent feature in the pump–probe signal.

I. Introduction

Chemical reaction dynamics in condensed phases involve the interaction between the “system”—the reactants and products of the reaction—and the “bath” of solvent molecules in an essential way. The relative diffusion of reactant species, the thermal activation of the system up the barrier to reaction, the crossing (and recrossing) of the transition state, and the stabilization of highly excited products are all strongly affected by system-bath coupling and energy transfer.¹ While overall chemical transformations may progress on a broad range of time scales, they are built up from individual elementary steps which occur on the ultrafast time scale of molecular vibrations, rotations, collisions, and electronic transitions.

Molecular photodynamics in rare gas solids provide a simple prototype of reactive dynamics in condensed media in general. Because of their simplicity, these model systems hold the promise of enabling the study of many-body processes with unprecedented detail. The classic problem of the cage effect upon photodissociation in condensed phases serves as an illustrative example for testing the information content in such investigations. The study of caging of I₂ and other molecules following photodissociation in condensed phases has a long history. Early work in the liquid and solid phases have provided an indirect view of the caging process through time-independent measurements of photodissociation quantum yields and their dependence on solvent mass, temperature, viscosity, excitation energy, and other parameters.^{2–5} More recently, ultrafast time-resolved experiments have begun to provide direct information on the dynamics of photodissociation and recombination.^{1,6–20} As an important compliment to experimental studies, molecular dynamics simulations of photodissociation and subsequent relaxation to equilibrium have revealed much information about the underlying microscopic dynamics in these systems.^{1,17–23} Photodissociation studies have also been performed on clusters,^{24–37} which provide finite analogues of true condensed phases.

We have recently initiated investigations of the photodissociation of I₂ in cryogenic matrices of Ar and Kr. The first studies of the system, which have already been reported,^{17–20} served to demonstrate that the caging process, i.e., the breaking and remaking of the I₂ bond within the isolation site of the host, can be followed in real time. Moreover, by performing molecular dynamics simulations in parallel with the experimental studies, it was shown that features in the pump–probe observable could be unambiguously assigned to dynamical events, such as the stretching of the I–I bond, the collision of the photofragments with the rare-gas cage, photofragment recoil, recombination, and subsequent coherent vibrations and vibrational relaxation of the molecule in its bound potential.

The information content of these experiments is directly related to the extent of classical coherence in the atomic motions. The existence of coherence is, in turn, dictated by a number of considerations. These include the initial preparation of the system, involving pump-pulse characteristics and the multi-dimensional surfaces involved in the pump transition; the experimental spatial and temporal resolution, which are dictated by the probe pulse width and the difference potentials involved in the probe transition; and, most importantly, the intervening dynamics between pump and probe configurations.

Ultrafast pump–probe experiments have the ability to follow a reaction coordinate into regions that are far removed from the vertically accessible Franck–Condon region. This occurs because these experiments measure *classical* correlations—a spatial “coherence” at the squared amplitude level of the initially prepared wave packets. This is to be contrasted with coherent spectroscopies, of which absorption and resonant Raman are examples, which probe phase correlations at the probability *amplitude* level.³⁸ In condensed media, such phase coherences are usually lost on time scales shorter than a vibrational period (~100 fs), over which, for instance, a liquid may not be distinguishable from a frozen glass. The spectroscopy of matrix isolated I₂ is a good case in point. Due to strong electronic dephasing, the vibronic absorption spectra of the molecule show no vibrational resolution.^{39,40} The analysis of the resonance

[⊗] Abstract published in *Advance ACS Abstracts*, May 1, 1995.

Raman spectra,⁴¹ which have been known for some time and show long overtone progressions in some spectral regions,⁴² indicate that dephasing of the prepared states is complete prior to completion of a single vibrational period. This situation also prevails in simple liquids, such as liquid Xe, in which the most recent resonant Raman data have been scrutinized to extract information about electronic predissociation.⁴³ Nevertheless, the information content is limited to time scales of a few hundred femtoseconds. A detailed understanding of the bath response to ultrafast dynamics of reactive species and the corresponding effect of the bath on the system are essential ingredients to the problem of condensed-phase chemistry. The chemically relevant processes occur on time scales of picoseconds or less, while the distance scales are on the angstrom range. Unlike conventional frequency domain experiments, ultrafast pump-probe measurements allow these scales to be viewed directly.

In this paper, we wish to emphasize that time-resolved pump-probe measurements can yield a detailed description of coupled system-solvent motions. With experimental time resolution that is somewhat shorter than our previous studies,¹⁷⁻²⁰ we observe that the coherence in the vibrational motion of the newly formed I₂ bond created by cage-induced recombination lasts—and is measurable over—a sufficiently long period to allow a detailed dynamical analysis of the signals. This allows us, through comparison with molecular dynamics simulations, to extract the local lattice cage motions that are directly coupled to the I₂ coordinate. This in turn enables the detailed study of the highly nonlinear dynamics of the driven lattice, which is a fascinating subject in itself.⁴⁴

In our previously reported time-resolved measurements of the caging of I₂ in solid Ar, the time resolution (cross correlation between pump and probe pulses) was 180 fs fwhm.^{17,18} In those studies, it was shown that the signal exhibited modulations that lasted for many picoseconds. It was clear, however, that the depth of the modulation was limited by experimental resolution. With only a modest improvement in time resolution to 150 fs cross correlation, little change is observed in Kr,²⁰ while a significantly deeper modulation of the pump-probe signal is obtained in the case of Ar. We present this higher resolution Ar data in this paper, along with a detailed analysis of both the observed signal and the accompanying (but experimentally inaccessible) atomic-scale processes revealed by molecular dynamics simulations. Comparisons of the measured and simulated observables are made, in both the time and frequency domains. We find that the simulations provide a good reproduction of most of the details seen in the measured signal. We then perform a microscopic analysis of the many-body trajectories to yield insight into the physical processes underlying the observed features of the signal. In particular, we focus on the signatures of the process of *recombination*. In what follows, we make the reasonable definition of recombination as the permanent vibrational deexcitation of the I₂ molecule below its gas-phase A state dissociation threshold.

The organization of this paper is as follows: In section II, we briefly describe the experimental method used to obtain pump-probe signals. Section III orients the reader by addressing the general physical process of photodissociation and recombination in this system from a qualitative perspective. Section IV provides experimental data resulting from the pump-probe experiments for several pump wavelengths. In section V, the simulation methodology used to model the experimental signals is presented. In section VI, a detailed discussion of the photodissociation-recombination dynamics is given. Comparison between simulation and experiment is made, and microscopic analysis of individual trajectories is performed to yield insight into the ultrafast many-body dynamics underlying

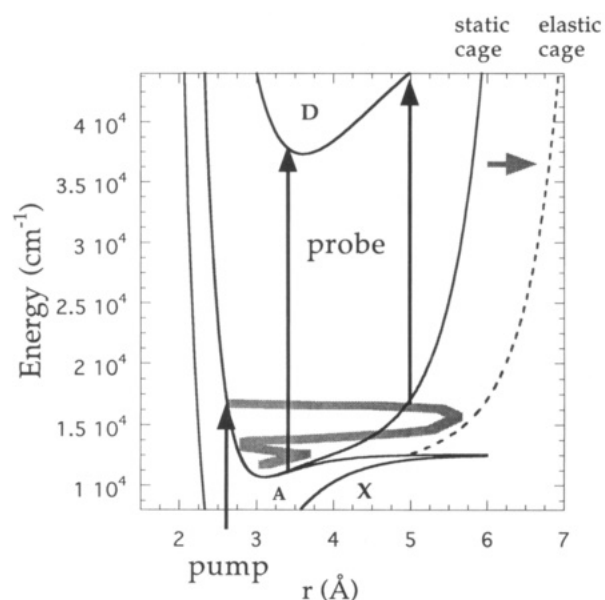


Figure 1. Schematic one-dimensional view of the pump-probe photodissociation dynamics, represented in terms of the I-I bond coordinate. See the text for discussion.

the experimental observables. Finally, some concluding remarks are given in section VII.

II. Experimental Section

The experimental approach has already been described in detail.¹⁷⁻²⁰ Briefly, a premixed gaseous sample of I₂ and Ar at a mole ratio of 1:5000 is condensed on a cold window, under conditions that guarantee isolation of the molecule and transparency of the film. At pump wavelengths between 640 and 740 nm, I₂ (A) is prepared on its repulsive wall at energies of 1000–3000 cm⁻¹ above the dissociation limit of the bare molecule. The second harmonic of the pump is used to probe the time evolution of the prepared wavepacket, via laser-induced fluorescence from the ion-pair states. The improved time resolution in these experiments, as short as 120 fs, is obtained by several adjustments to the optical train, including the use of reflective optics wherever possible, the use of a 200 μm thick BBO crystal for second harmonic generation, and a nearly collinear overlap between the pump and probe beams. The experimental time resolution is determined by the signal that results from the first passage of the initially prepared wavepacket over the “inner” resonance window (see below). The dispersion of the initially prepared wave packet is rather small in this excursion, and, although a lower limit, the reported time resolution is well-determined. This has been directly verified in the case of measurements with an angle between the pump and probe beams by simultaneously recording the signal and cross correlation between pump and probe beams by difference generation.

III. Photodissociation-Recombination Dynamics

Figure 1 shows a schematic one-dimensional view of the pump-probe photodissociation dynamics, represented in terms of the I-I bond coordinate. Centered at $t = 0$, a pump pulse of approximately 100 fs duration excites the system from its ground to an excited electronic state. Although in principle the electronic states of the full system involve many nuclei, to a good approximation, we can think of the electronic excitation as being localized on the impurity molecule, corresponding to the promotion of I₂ from its ground X (¹Σ_g⁺) to its excited A (³Π_u) state. The X and A states of I₂ are shown in Figure 1. The vertical excitation of I₂ at wavelengths between 640 nm and 740 nm could, in principle, lead to the repulsive walls of

both the $A(^3\Pi_{1u})$ and $A'(^3\Pi_{2u})$ molecular potentials. However, based on the known radiative lifetimes of $A' \rightarrow X$ and $A \rightarrow X$ transitions in solid Ar,^{17,39,40} it can be inferred that the absorption probability to the A state is 2–3 orders of magnitude larger than it is to A'. Thus, we can be confident that the pump pulse prepares a wave packet on the repulsive wall of the A state, above its gas-phase dissociation limit.

The A state of I_2 is weakly bound by 1890 cm^{-1} , and with the wavelengths considered in the present work, the system finds itself on the inner repulsive part of the A potential surface with $1000\text{--}3000\text{ cm}^{-1}$ of excess energy above dissociation limit of the bare molecule. Following excitation by the pump pulse, the I fragments move apart as the excess potential is converted to kinetic energy. In the gas phase, the I atoms would separate to infinity, yielding a unit probability of photodissociation. In the solid, however, the Ar lattice atoms prevent permanent dissociation by "caging" the photofragments. Unlike the case in liquids^{1–15} and van der Waals clusters,³⁵ cage-induced recombination of I_2 proceeds with unit probability in matrices of Ar and Kr.

The caging by the lattice involves complex many-body dynamics of the I_2 and surrounding Ar atoms on an ultrafast time scale. It is nevertheless useful to approximate the lattice, at least conceptually, by a one-dimensional effective potential along the I_2 vibrational coordinate. Such a representation is indicated in Figure 1 as the "static cage" potential. This curve consists of the bare I_2 (A) potential plus the sum of I–Ar interactions as a function of I–I bond length, calculated with the Ar atoms held at their equilibrium positions. The I–Ar collisions involved in the caging process, however, will not leave the Ar atoms at their initial positions (as we will detail below), and thus the static cage is only a crude approximation. A perhaps better—but still approximate—one-dimensional model is to view the many-body lattice as presenting an "elastic cage", which embodies the expansion and deformation of the local lattice environment by the photodissociation event. This expectation is illustrated schematically in Figure 1: the I_2 bond length extends beyond the limit allowed energetically by the static cage potential, causing the cage to dilate, and the photofragments are ultimately deflected by the elastic cage potential and induced to recombine. As we shall emphasize below, however, this one-dimensional view neglects important details of the many-body dynamics of the molecule and lattice occurring on the time scale of photodissociation and recombination.

At some point following the collision of the I fragments and the Ar cage, the I_2 vibrational energy drops below its dissociation threshold, and thus recombination has occurred. The re-formed I_2 molecule then undergoes vibrational relaxation on the A electronic surface. Although radiative or nonradiative electronic relaxation is expected to occur eventually, during the time scale of relevance to the present experiments, no detectable nonadiabatic transitions to the X or A' states are observed. We can thus think of the photodissociation–recombination dynamics as occurring adiabatically on the single A electronic surface.

To interrogate the photodissociation and recombination processes, the system is subjected to a probe pulse, which is generated by frequency doubling a delayed copy of the pump pulse. Thus, the pump and probe energies move in tandem as the pump wavelength is varied. The probe creates a further electronic excitation in the system, which can be thought of approximately as the promotion of the I_2 from the A state to a (solvated) ion-pair state. There is a dense manifold of ion-pair states, which are typified by the D state; a Rittner form of the D state,⁴⁵ shifted in energy by solvation in the Ar lattice,⁴⁶ is

shown in the Figure. The experimental observable is the laser-induced fluorescence from this state as a function of pump–probe delay.

Assuming the classical Franck approximation,⁴⁷ absorption of the probe photon by the I_2 (A) molecule will occur when the difference potential $\Delta V = V_D - V_A$ is equal to the photon energy. Here, V_D and V_A are the many-body potential surfaces correlating to the I_2 D and A gas-phase electronic states, respectively. To accurately estimate the resonance configurations, these potentials must include the effect of the lattice on the bare I_2 molecule, at least qualitatively. The approximate conceptual view we adopt and show in Figure 1 is to consider dynamics on the bare A state plus an effective one-dimensional cage wall and probe excitation to the ion-pair state solvated by an equilibrium lattice. (The real situation is much more complicated, as each electronic energy depends on the positions of *all* the atoms in the system.) It is clear from the figure that there are *two* distinct I_2 bond lengths which yield a vertical transition resonance.¹⁷ This provides two "windows" on the photodissociation–recombination dynamics, which we shall refer to as the "inner" and the "outer" resonance conditions, respectively. The two windows provide complimentary views of the A state dynamics: The inner window probes relatively small-amplitude vibrational dynamics of I_2 , while the outer window provides information on the caging process itself.

IV. Results

We now turn our attention to the experimental data. In Figure 2, we show the pump–probe signals measured for several pump wavelengths. The wavelength range considered is the same as in our previous study.¹⁷ In our discussion below, we characterize each pump–probe measurement by the pump wavelength; the frequency-doubled probe pulse energy is then determined. At 640 nm, only the inner window contributes to the signal, as the resonance condition creating the outer window has moved to regions of configuration space that are not accessed by the dynamics. At all other wavelengths both windows contribute, with the outer window resonances being limited to the first picosecond following photodissociation. At the longest wavelength, 740 nm, the outer window contribution results in two well-resolved peaks, which are indicated in Figure 2a. The first peak in all the signals results from the first passage of the prepared wavepacket through the inner window. The full width at half-maximum of this peak is taken as the experimental time resolution. The first recursion to the inner window occurs after a delay of ~ 1 ps. This recursion occurs after collision of fragments with the cage and accompanying loss of kinetic energy, and the trajectories recross the inner window at a reduced velocity. The magnitude of the signal is related to the dwell time of the trajectories in the resonance window (in other words, the inverse of the instantaneous velocity in the window), and thus the intensity under the ~ 1 ps peak relative to the intensity of the first passage provides a measure of the energy loss at the cage wall. For example, by comparison of intensities in the 740 nm data, it can be inferred that approximately 40% of the total kinetic energy (excess plus binding energy at the resonance window) is lost during the first cage collision.

It is apparent in Figure 2 that all of the signals oscillate, with a period of approximately 400 fs, for times past the first recursion to the inner window. For the longest wavelength considered, $\lambda_{\text{pump}} = 740\text{ nm}$ (corresponding to the smallest excess energy above the A state dissociation threshold, $E_{\text{excess}} \approx 1000\text{ cm}^{-1}$), the oscillations are deep and are visible for several picoseconds—as long as signal is observed. As the wavelength is shortened, resulting in increased excess energy of the I photofragments, the depth of the oscillations decreases.

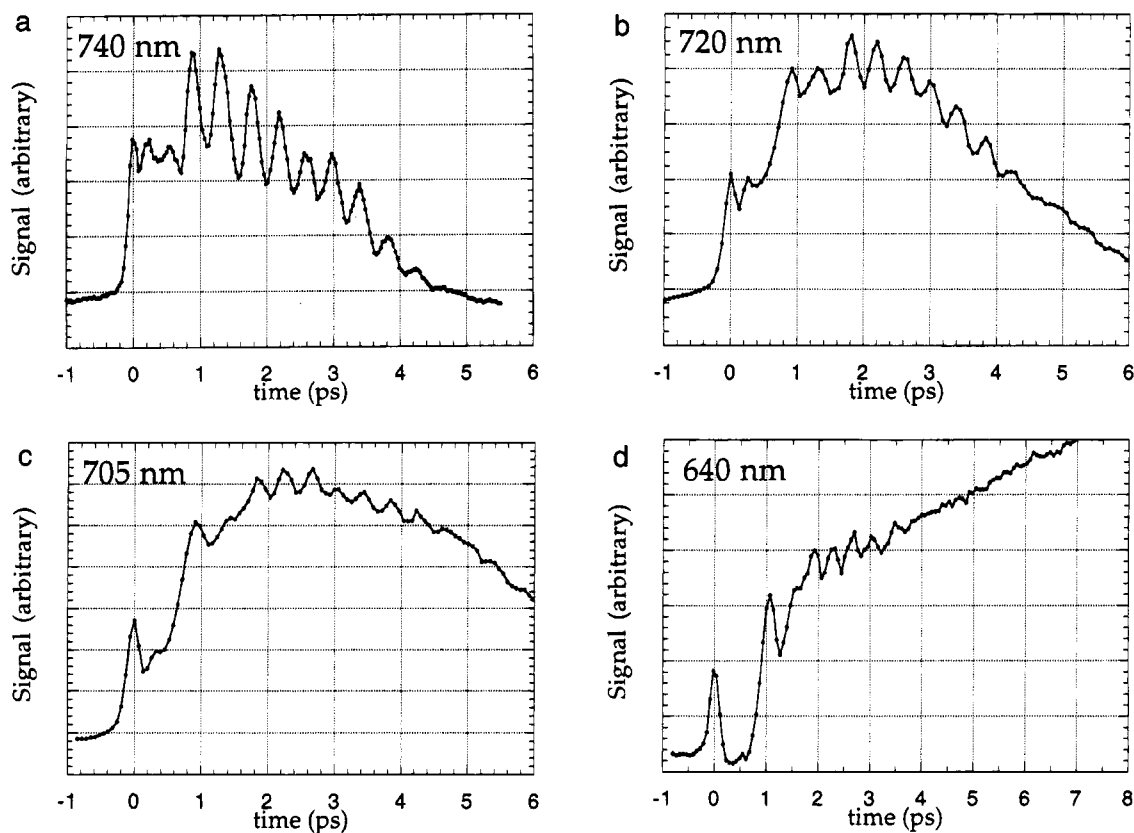


Figure 2. Experimental pump-probe signals for several wavelengths. (a) 740, (b) 720, (c) 705, (d) 640 nm.

Coherent oscillations in the pump-probe signal are, however, visible for all excess energies considered, up to $E_{\text{excess}} \approx 3000 \text{ cm}^{-1}$ for $\lambda_{\text{pump}} = 640 \text{ nm}$. While regular oscillations with a period of $\sim 400 \text{ fs}$ are discernible in these traces, the amplitude of these oscillations is highly modulated. These modulations are completely reproducible for a given pump-probe wavelength and arise from coupling of the I_2 vibration to specific modes of the bath, which are initially driven by the dissociation process. While the characteristic frequencies of the modes that couple back along the I-I coordinate can be extracted from the experimental signals, the experiment does not yield a direct identification of the underlying collective motions. The nature of these modes can, however, be identified through comparison with simulations.

The data shown in Figure 2 contains a great deal of detailed information about the underlying photodissociation-recombination dynamics encoded in the vibrational coherence. The vibrational coherence is *created* by the interaction between the photofragments and the many-body cage. In the absence of lattice caging, *no coherence would be observed*. This is in marked contrast to the previous observations of vibrational coherence in condensed phases by Ruhman and coworkers for I_3^- photodissociation in ethanol solution,²³ and Hochstrasser and co-workers for HgI_2 photodissociation in solution.⁴⁸ In both of those studies, an *intact* vibrationally excited fragment, I_2^- and HgI , respectively, remain behind after an I atom is lost during photodissociation. In the present study, however, the coherently oscillating fragment is, for a brief time, actually in a dissociated state, with the guest-host interactions controlling the subsequent spatial coherence of the recombination dynamics.

In molecular iodine, 10 electronic states converge to the asymptotic limit of $\text{I}(^2\text{P}_{3/2}) + \text{I}(^2\text{P}_{3/2})$, of which several are known to have shallow wells in the gas phase.⁴⁹ Thus, upon dissociation and recombination of I_2 , the possibility of mixing among different electronic surfaces exists. Despite these considerations, our single surface molecular dynamics simula-

tions have been quite successful in reproducing the observed dynamics in solids.¹⁷⁻²⁰ Moreover, in contrast with liquid¹ and cluster³⁶ environments, it has been ascertained that the molecular X state is not populated in the caging process.^{17,20} The latter observation has been taken to imply that, in the constrained environment of the solid cage, the configurations where the A and X surfaces coalesce are not reached.¹⁶⁻¹⁹ With the limited time resolution of the previous experiments, it was not possible to establish whether the observed dynamics were strictly adiabatic, or whether the recombination occurred over both A and A' states. As is well known in the case of excitation to the B state,^{39,40,46,50} when excited to the A state, we observe vibrationally relaxed emission from both A and A' which are distinguished by their different radiative lifetimes.^{46,50} Thus, recombination eventually leads to population of both of these nested states. The timing and location of the crossing between these states remains an open question. Time-resolved photo-selection experiments are well suited to address this issue. Pump-probe experiments provide the means for three-step photo-selection by controlling the polarization between pump and probe beams, and by monitoring the polarization of the fluorescence.^{51,52} A detailed analysis of such measurements will be given elsewhere. Here we provide the experimental evidence for the validity of the assumption that *the observed dynamics proceeds adiabatically*. This is the assumption upon which hinges the validity of the classical molecular dynamics simulations, which use a single electronic potential energy surface and upon which we rely for our interpretations.

In Figure 3 we show normalized traces of data taken at $\lambda_{\text{pump}} = 736 \text{ nm}$, obtained by monitoring total on-axis fluorescence with parallel and perpendicular polarizations between pump and probe beams. The intensity ratio between these two different geometries, which is determined by the directions of the transition dipoles involved in the three different steps, does not interest us in the present. What is of interest is the observation that the details of the time profiles are identical in the two cases.

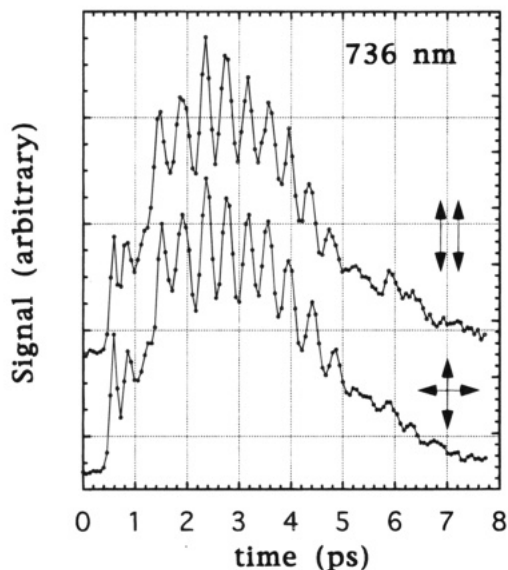


Figure 3. Polarization dependence of the pump-probe signals for pump wavelength of $\lambda_{\text{pump}} = 736$ nm. The relative pump-probe polarization is indicated schematically by the parallel or crossed arrows adjacent to the corresponding signals.

If the initially prepared population were to partition between two electronic surfaces, then time dependent variations in the modulated signals would result in the photoselected experiment. The absence of such a variation is strong evidence that, for the observation period of ~ 7 ps, the dynamics are strictly adiabatic and thus constrained to the I_2 (A) surface. Presumably, the A' state is populated at some later time, from A ($\nu < 10$) states. This conclusion is in accord with the suggestion of Böhling et al., which was based on the observation that the relative fluorescence intensities from vibrationally relaxed A and A' states in matrices is independent of the cage size.⁵⁰ It had previously been argued that if the partitioning between these surfaces is controlled by the extent of separation between the atoms prior to recombination, then their relative populations would be correlated with the size of the isolation cage.³⁹

Despite the rich information content in the experimental data of Figures 2 and 3, the signals are the result of complex many-body nonlinear dynamics, the details of which cannot be extracted by a cursory examination of the experimental data. It is essential to combine the experimental studies with theoretical simulations to yield a comprehensive understanding of the signals and their underlying dynamics. The characteristics of the present system, especially the absence of nonadiabatic electronic transitions, makes this an ideal case for such an approach.

V. Molecular Dynamics Simulations

To model and interpret the measured pump-probe signals, we carry out classical molecular dynamics simulations⁵³ and generate the predicted observable using the classical Franck approximation.⁴⁷ A single I_2 is inserted into a double-substitutional site of an Ar face-centered cubic lattice. The infinite system is approximated by 500 atoms using periodic boundary conditions.⁵³ The many-body potentials of the X and A electronic states are approximated as pairwise additive. The I-I interaction on the X and A states are represented by Morse potentials with appropriate parameters. The Ar-Ar interaction is modeled by a Lennard-Jones potential, as are the I-Ar interactions. Standard values are chosen for the Ar-Ar Lennard-Jones parameters.⁵³ The I-Ar parameters are approximated by those appropriate for Xe-Ar.⁵⁴ These non-bonded interactions are assumed to be the same in the ground

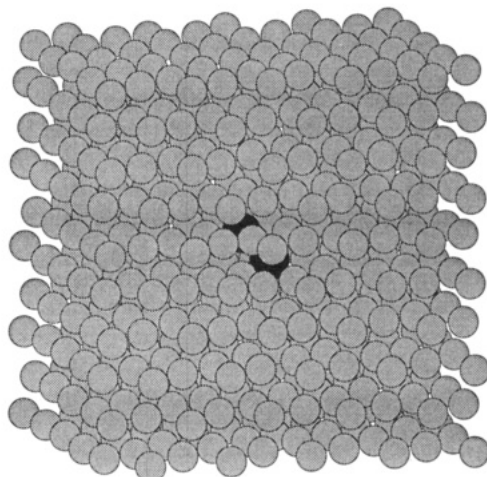


Figure 4. Molecular dynamics box used in the simulations. The box contains 500 atoms: 498 Ar atoms and 2 I atoms. Lattice atoms have been removed to expose the I_2 molecule, which is the darker object visible at the center of the cell, aligned along the [111] direction of the crystal.

TABLE 1: Potential Parameters Used in the MD Simulations

potential parameters	values
D_e (A state)	1840 cm^{-1}
r_e (A state)	3.10 Å
β (A state)	2.147 Å ⁻¹
$\epsilon_{\text{Ar-Ar}}$	83.26 cm^{-1}
$\sigma_{\text{Ar-Ar}}$	3.405 Å
$\epsilon_{\text{I-Ar}}$	130.24 cm^{-1}
$\sigma_{\text{I-Ar}}$	3.617 Å

and excited electronic states. This is an approximation, and we are currently exploring the effects of different system-solvent interactions in different electronic states on nonadiabatic dynamics. Here, these effects should not be important, as experiments indicate that the photodissociation-recombination dynamics occur adiabatically on the A surface. The potential parameters used are given in Table 1. A cutaway of the resulting molecular dynamics box, exposing the I_2 situated at the center and aligned along the [111] direction in the fcc crystal, is shown in Figure 4.

The observed signals are modeled by integrating ensembles of classical trajectories, with initial conditions approximating those relevant to the pump-probe experiment. We are attempting to capture classically the spatial coherence of an evolving quantum wave packet. The initial dispersion of the ensemble has a strong influence on the subsequent localization of the dynamics in phase space and thus care must be taken in selecting the initial conditions of the classical trajectories. The following method is employed: The ensemble is first equilibrated at a prespecified temperature (see below) using the $I_2(X)$ state parameters by periodically rescaling the particle momenta while integrating ground (X) state trajectories. Initial configurations are randomly chosen from the equilibrated set with the condition that the I_2 bond length satisfies the desired Franck-Condon resonance condition to within the bandwidth of the excitation pulse. At $t = 0$, the I_2 potential is switched from the X to the A values (see Table 1). The I_2 relative momenta are further adjusted by generating Gaussian random variables with zero mean and standard deviation corresponding to the Wigner function⁵⁵ calculated from the harmonic approximation to the ground state vibrational wave function of the X state, and adding the resulting momentum to that already present from the thermalization. This step increases the dispersion of I-I relative momentum and is done to model the momentum uncertainty inherent in the ground X state vibrational wave function. Note

that each trajectory undergoes $X \rightarrow A$ excitation at the same time, taken to be $t = 0$. The finite duration of the pump (and probe) pulse is taken into account later, when the final observable is convoluted with the pump–probe cross correlation function (see below). Physically, this smears out both the starting time of the trajectories over the 100 fs pump pulse and the finishing time determined by the 100 fs probe interaction. Following the initial excitation, Hamilton's equations are integrated to propagate the dynamical variables, which are written periodically to disk for subsequent analysis. Ensembles of 100 trajectories are employed in the simulations presented here.

The experimental data presented in this paper were obtained at a temperature of 15 K. At these cryogenic temperatures, the zero point energy of each Ar atom is comparable to its thermal energy, and thus fluctuations in lattice atom positions due to quantum uncertainty can potentially play an important role. This can be taken into account approximately by a scaling of the classical temperature.⁵⁶ To match with experiments at temperature T , the classical system is simulated at an artificially elevated temperature T' , given by:

$$T' = \frac{\hbar\omega}{2k_B} \left(\tanh\left(\frac{\hbar\omega}{2k_B T}\right) \right)^{-1} \quad (1)$$

Using the Debye frequency of solid Ar, $\omega = 65 \text{ cm}^{-1}$, a scaled temperature of $T' = 40 \text{ K}$ is obtained and was employed in the simulations. The qualitative character of the simulations is not sensitive to the particular value of T' chosen. See ref 20 for a discussion of the effect of temperature on simulations of I_2 photodissociation in solid Kr.

To simulate the observable signal, we invoke the classical Franck principle,⁴⁷ which approximates optical excitation as a vertical process occurring at nuclear configurations for which the difference potential between the initial and final electronic state equal the probe photon energy. The electronic energies in general depend on the positions of all the atoms of the system. We approximate the many-body potentials by an effective one-dimensional representation and assume that the resonance conditions depend only on the I_2 bond length R . Thus, for excitation from A to D by the probe pulse:

$$\Delta V(R) = V_D(R) - V_A^{\text{eff}}(R) = h\nu_{\text{probe}} \quad (2)$$

Here $V_D(R)$ is the solvated ion-pair potential, while V_A^{eff} is the A state Morse potential plus an effective one-dimensional cage potential, as discussed in section II. Due to the form of the two potential curves (see Figure 1), there are two roots to eq 2, which provide two "windows" on the photodissociation–recombination dynamics. The positions of these windows depend on the particular probe wavelength employed.

Given the two roots $R = (R_1^*, R_2^*)$ to eq 2, the pump–probe signal can be constructed by convolution of the pump–probe cross correlation function (taken here to be a Gaussian with a 150 fs fwhm) with a bare signal function, $S(t)$, given in the one-dimensional approximation by

$$S(t) \propto \int_{-\infty}^{\infty} \mu^2(R) \varrho(R,t) \delta[\Delta V(R) - h\nu_{\text{probe}}] dR \quad (3)$$

where $\mu(R)$ is the transition dipole, $\varrho(R,t)$ is the evolving classical probability density of I_2 distances, and the last factor is the energy-conserving δ function selecting the resonant configurations. This expression is just the classical Franck principle⁴⁷ for the trajectory ensemble with a time delay of t between instantaneous pump and probe pulses. The classical density approximates the quantum mechanical probability density, $\varrho(R,t) \approx |\psi(R,t)|^2$; for the heavy particles comprising

the present system, this is expected to be a reasonable approximation. In practice, $S(t)$ is calculated from the ensemble of classical trajectories using the expression:

$$S(t) \propto \frac{1}{N} \sum_{j=1}^N \frac{|\mu(R_j)|^2}{|\partial \Delta V(R_j) / \partial R|_{R_j}} \sum_{n=1}^N G[R_j^* - R_n(t)] \quad (4)$$

Here $G(R)$ is a Gaussian function of R , whose purpose is to provide a smooth, continuous representation of $\varrho(R,t)$ from the singular density corresponding to an ensemble of individual trajectories. We choose the spatial width of $G(R)$ to correspond to $|\psi|^2$ of the A state ground vibrational wave function. The reason behind this somewhat arbitrary choice is that if vibrational relaxation goes to completion in the A state, leaving motionless trajectories (neglecting thermal fluctuations), resulting $\varrho(R,t)$ becomes the ground A vibrational state quantum probability density. The final results are not particularly sensitive to small changes in this width. The evolving vibrational probability density is thus approximated as a "swarm" of Gaussians centered on each trajectory in the ensemble, and the signal resulting from a probe pulse at time t is the sum of the contributions from each evolving Gaussian evaluated at the two probe windows, weighted by the square dipole moment and a density of states factor, resulting from the change of variables in the delta function of eq 3. It should be noted that although the width of $G(R)$ is fixed, the density $\varrho(R,t)$ can still freely spread, by dispersion of the underlying individual trajectories. Finally, to generate the predicted observable $\sigma(t)$, the bare signal function is convoluted with $W(t)$, the pump–probe cross-correlation function:

$$\sigma(t) = S(t) * W(t) \quad (5)$$

The main approximation in this treatment is the representation of the multidimensional potential hypersurfaces as an effective one-dimensional curve. Although this is a good approximation for the recombined I_2 around the inner window where the relatively small amplitude vibration of the diatomic does not strongly perturb the lattice, for the initial collision with the cage near the outer turning point, this picture can break down strongly, and the detailed dynamics along the I–Ar coordinates should be considered more explicitly.

In the above formulation, we have ignored the finite spatial width of the resonance windows. The temporal resolution of the detected coherences depends on the width of the probe window, ΔR , or, equivalently, the spatial resolution, which is inversely proportional to the probe laser pulse width, Δt_L . For a probe resonance window located at R^* , the spatial resolution is determined by the ratio of the spectral width of the laser and the gradient of the difference potential at the probe resonance. For a one-dimensional system, this becomes

$$\Delta R \approx \frac{\Delta E_L}{(\partial \Delta V / \partial R)_{R^*}} \approx \frac{\hbar}{\Delta t_L (\partial \Delta V / \partial R)_{R^*}} \quad (6)$$

Near the inner window resonance, the gradient of the difference potential is $\sim 4200 \text{ cm}^{-1}/\text{\AA}$. Therefore, for a probe pulse width of 100 fs, the spatial resolution (i.e., the width of the window) is $\sim 0.08 \text{ \AA}$ which is sufficiently small compared to the width of the evolving packet ($\sim 0.2 \text{ \AA}$ or larger, see below) to provide a complete spatial resolution and full modulation of the time-dependent signal. The observable modulation depth would be lost, due to reduction of the spatial resolution, if the probe pulse width were to be shortened by a factor of 3. Thus, contrary to what one might expect intuitively, the use of the shortest pulses available may *not* provide the most detailed

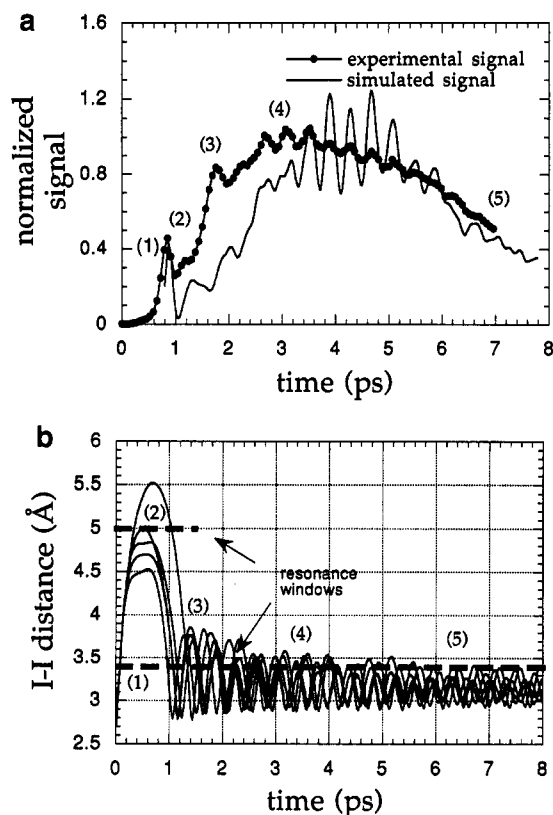


Figure 5. Comparison between the experimental and theoretical pump-probe signals for 705 nm pump wavelength. See the text for discussion.

information about the dynamics of the system. When the spatial resolution is comparable to the spatial coherence of the evolving dynamics, then an additional convolution of $S(t)$ by the window function is required. The need for such a treatment can be easily assessed from the experimental signals. In the present experiments, these effects can be ignored.

VI. Discussion

(a) Analysis of Time Profiles. In Figure 5a, we show a comparison between the experimental and theoretical pump-probe signals for the case of 705 nm pump wavelength. In synthesizing the observed signal from the trajectory data, the positions of the inner and outer windows were taken to be at $R_1^* = 3.4 \text{ \AA}$ and $R_2^* = 5.0 \text{ \AA}$, respectively. These values were determined by small variations of values predicted from the known A and D state potentials, including equilibrium solvation effects. The position of the inner window was adjusted to fit the long-time vibrational relaxation profile of the signal, resulting in a value quite close to that predicted from the Rittner form of the D state potential,⁴⁵ when shifted down in energy by its experimental equilibrium solvation in Ar. The long-time envelope of the simulated signal is extremely sensitive to the position of the inner window, providing a sensitive experimental avenue to determining the difference potential.²⁰ The outer window position was then determined by fitting the experimental data, yielding a reasonable value when the *effective* A state potential, including repulsive I-Ar interactions, is considered. In the absence of quantitative knowledge of the R dependence of the transition dipole in the solid, the relative weights of the inner and outer windows were somewhat arbitrarily taken to be in the ratio 2:1. As shown below, trajectories near the outer window contribute only a single, relatively small, feature to the overall signal, and thus the comparisons between experiment and theory are not very sensitive to the position of the outer window or the ratio of dipole moment values.

Although there are some significant differences in the magnitude of the experiment and the simulation, especially during the first few picoseconds following photodissociation, each notable feature in the experimental signal is reproduced in the simulation. In addition, nearly quantitative reproduction of the *timings* of each feature in the observed signal is achieved.

The close agreement between the simulated and measured signals is strong evidence that the molecular dynamics simulations are faithfully capturing the essential features of the many-body dynamics of the actual system. Unlike an experiment, however, the simulations provide complete microscopic detail of the dynamics. Taking advantage of this omniscience, we now turn our attention to analysis of the simulation data.

In Figure 5b, the simulation data for five trajectories selected randomly from the full ensemble are depicted. The Figure shows the I_2 bond length vs time for the trajectories. In addition, the two resonance conditions employed are indicated by the horizontal dashed lines. The Figure has been shifted to bring the zero of time in register with that of Figure 5a to allow direct comparison. Several key features of the observable signal are identified and numbered in Figure 5a. In Figure 5b, these features are correlated with the instantaneous dynamics of the I_2 .

The feature labeled (1) in Figure 5a is a sharp, instrument-response-limited peak in the signal occurring at very short pump-probe delay times. By considering the trajectory data in Figure 5b, this peak can be correlated with the rapid and highly spatially focused passage of the ensemble through the inner window. As the ensemble passes through this window, the signal rises and then falls, yielding a nonmonotonic response. At a time around 400 fs following this first peak, a second feature (2) is visible in both the experimental and the simulated signal. The trajectory data indicate that this transient maximum in the signal is the result of a cage-induced resonance occurring at the outer window. Approximately 500 fs later, a third peak, labeled (3), appears. This feature correlates with the coherent return of the trajectory ensemble to the inner window.

For several picoseconds following this early transient behavior, oscillations are visible in both the experimental and the simulated signal; this general feature is labeled (4) in Figure 5. The period of these oscillations is approximately 400 fs, and the timing of the minima and maxima of this modulation in the observed signal is very accurately modeled by the simulation. The trajectory data reveals that the oscillation is due to the coherent vibrational dynamics of I_2 , which persists for at least 6 ps. During the experiment, the envelope of the signal rises and then falls to zero at long times (beyond 8 ps). As the trajectory data reveals, the shape of this envelope is the result of the transfer of the I_2 energy into the lattice by vibrational relaxation, resulting in a decreasing amplitude of the I_2 oscillation. The preceding rise in the signal results from the coalescence of the I_2 turning point at the inner window position: the dwell of the trajectories in the resonance window is maximal when the turning point falls at the window. As the amplitude of the vibration decreases, the ensemble "falls out" of the window, eventually giving no probe absorption and thus no signal. This feature is labeled (5) in Figure 5. It should be noted that this effect is wavelength-dependent, and for shorter probe wavelengths, the inner window may fall near the minimum of the A state potential, yielding a nonvanishing plateau in the signal at long times.¹⁷

(b) Frequency Analysis. In Figures 6 and 7, time series analysis of the oscillatory part of both measured and calculated signals are presented, respectively, providing a further comparison between experimental and theoretical observables. This was accomplished by fitting the signals $\sigma(t)$ to a smooth fifth-

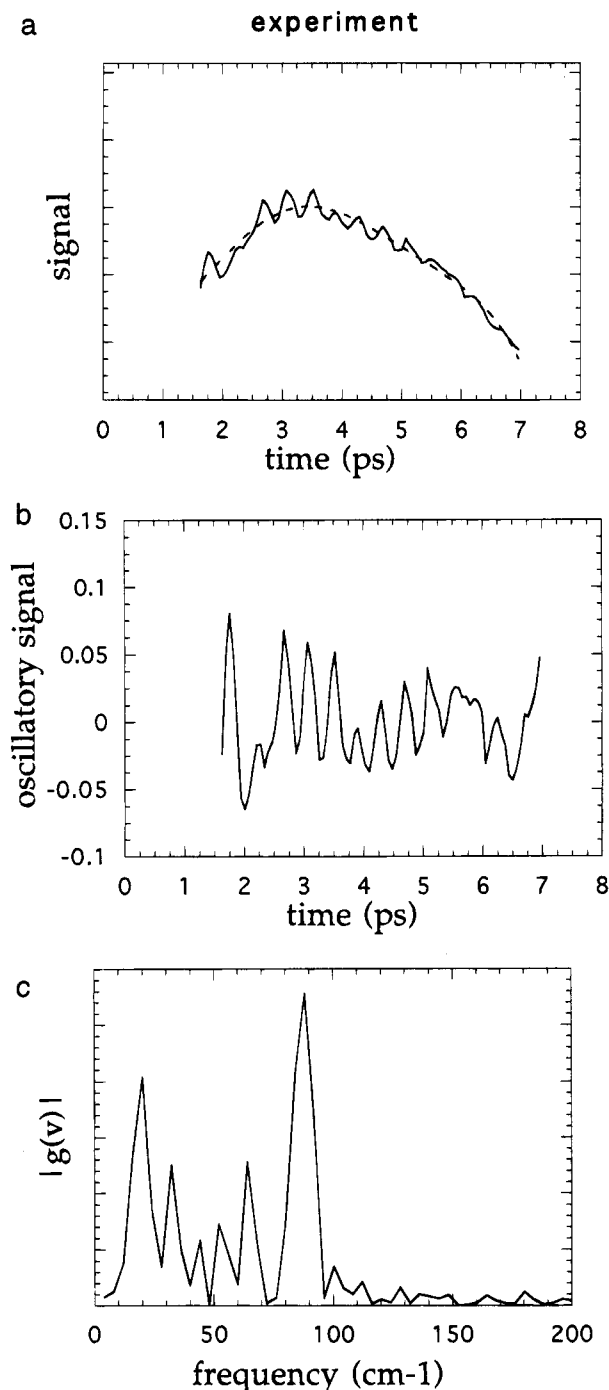


Figure 6. Time series analysis of experimental signal. (a) Signal for $t > 1.6$ ps, and smooth fit to a fifth-order polynomial. (b) Oscillatory part of signal, as defined in text. (c) Absolute value of Fourier transform of oscillatory part of signal. See the text for discussion.

order polynomial, yielding a smoothed signal $\bar{\sigma}(t)$. In the fitting, the initial transient aperiodic behavior is ignored, and only data for times greater than $t = 1.6$ ps following photodissociation are considered. The signals and their smooth approximations are shown in Figures 6a and 7a for the experiment and the simulation, respectively. A normalized oscillatory signal $\xi(t)$ is then computed:

$$\xi(t) = \frac{\sigma(t)}{\bar{\sigma}(t)} - 1 \quad (7)$$

and Fourier transforms of $\xi(t)$ calculated to reveal the characteristic frequencies underlying the observable signal. In Figures 6b,c, the oscillatory signal and the absolute value of its Fourier transform are shown for the experimental data; the correspond-

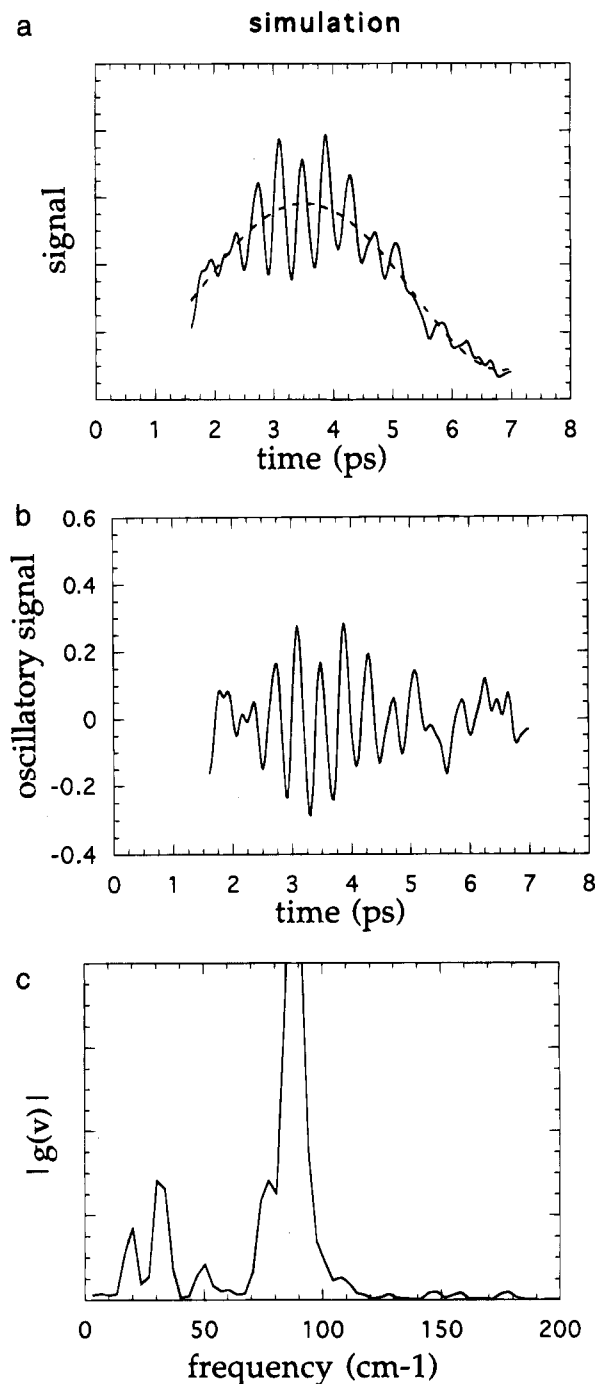


Figure 7. Time series analysis of simulated signal. (a) Signal for $t > 1.6$ ps, and smooth fit to a fifth-order polynomial. (b) Oscillatory part of signal, as defined in text. (c) Absolute value of Fourier transform of oscillatory part of signal. See text for discussion.

ing results from simulation are given in Figure 7b,c. Although there are qualitative differences between the two spectra, especially in the relative amplitudes of the observed features, the major peaks in both agree qualitatively. The most prominent feature in both spectra is the peak corresponding to the I_2 vibration, centered around $\nu = 85$ cm⁻¹. In addition, several lower frequency features are observable in both spectra. These peaks, ranging from 15 to 65 cm⁻¹, correspond to the modulation of the signal by lattice vibrations. Note that 65 cm⁻¹ corresponds to the Debye frequency of solid Ar. The origin of the 15 cm⁻¹ peak is evidently a collective motion of the cage which is strongly coupled to the I-I coordinate.

Although the physical mechanism underlying the appearance of lattice motion in the signals in the experiment and simulation are undoubtedly somewhat different, as we have ignored, for

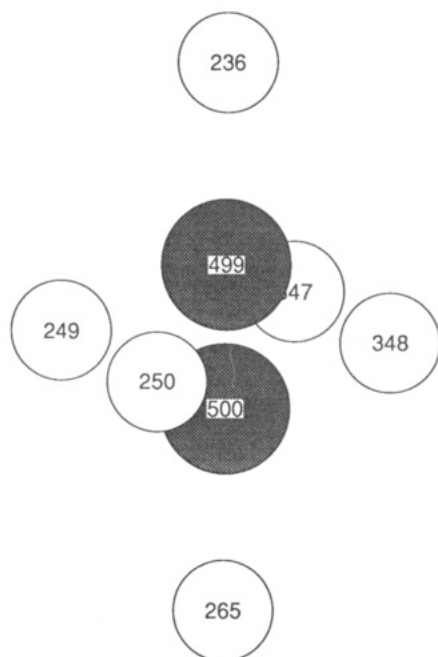


Figure 8. Local structure of the Ar lattice immediately around the I_2 impurity. Each atom is numbered for reference in the text.

instance, the modulation of the ion pair solvation energy (and thus the difference potential ΔV) by the instantaneous lattice configuration, the qualitative agreement of the experiment and the simulation at the level of observable signal suggests that the A state *dynamics* are being well-modeled within the approximations we are employing. Adopting this viewpoint, we now turn our attention to a detailed analysis of individual trajectory data, to gain insight into the many-body dynamics of caging and recombination upon photodissociation in this system. We will focus our attention on the dynamics of the 705 nm ensemble for most of the discussion.

(c) Trajectory Analysis. In Figure 8, we show the local structure of the Ar lattice immediately around the I_2 impurity. It can be seen that the six Ar atoms that are nearest neighbors of the I_2 form a distorted octahedron. Each atom is numbered in Figure 8 for reference in the discussion below.

In Figure 9a, we show the I_2 vibrational energy for a trajectory from the 705 nm ensemble as a function of time. Although this trajectory is only one member of the ensemble, it is representative of commonly observed behavior. In Figure 9b, the corresponding I_2 bond length vs time is given, along with the deviation from equilibrium of Ar atom (265), projected along the [111] direction in the crystal. As indicated in Figure 8, this atom is immediately adjacent to the I_2 and situated along the [111] axis.

The I_2 loses virtually all of its excess kinetic energy during the first 500 fs following dissociation, as indicated in Figure 9a. Figure 9b shows that this energy loss occurs during the I_2 bond extension and concomitant collision of the I atoms with the Ar cage. The effect of this collision on an adjacent Ar atom is also visible: following a slight lag in time, a sudden shift in position of the atom occurs, which closely tracks the extension of the I_2 bond. While the I–I distance is near its maximum excursion of approximately 5.6 Å at $t = 500$ fs, the Ar undergoes an oscillation around a new, shifted equilibrium position. Following this, both the I_2 and Ar modes begin a return to their initial positions.

During this compression of the I_2 bond, occurring between $t = 750$ fs and $t = 1400$ fs, the I_2 energy is observed to *increase*. This energy flow back into the molecule from the lattice is substantial, on the order of 500 cm^{-1} . Thus, as the molecule

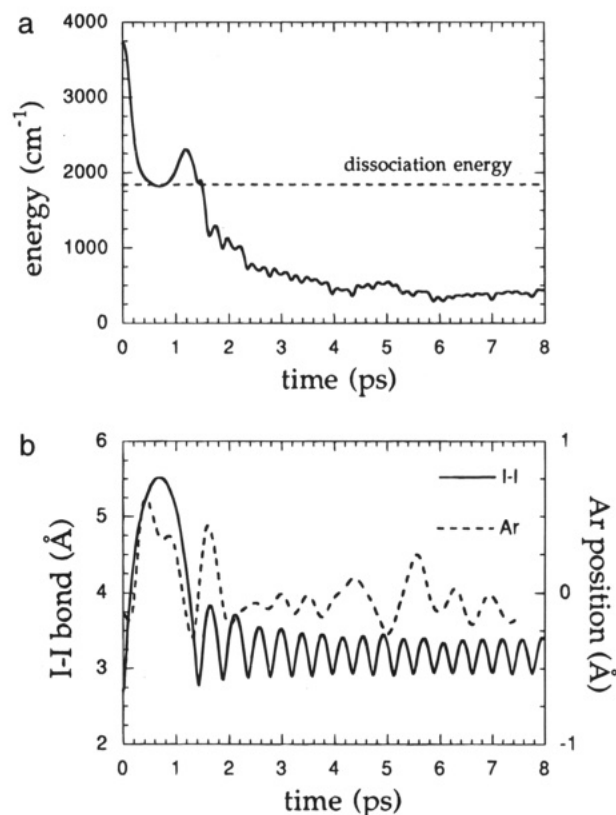


Figure 9. Trajectory data for a representative trajectory from the 705 nm ensemble. (a) I_2 vibrational energy as a function of time. (b) I_2 bond length vs time and dynamics of adjacent Ar (265). See text for discussion.

reaches its first inner turning point following photodissociation, there are still several hundred wavenumbers of excess energy in the molecule. In other words, based on an energetic criterion, the molecule *has not yet recombined!* Permanent I_2 recombination does not occur until the *second* bond extension, approximately 1.4 ps following photodissociation, when a second pair of I–Ar collisions (one for each I–collinear Ar pair) brings the I_2 energy permanently below the dissociation threshold.

The simulation data indicate that recombination is a subtle process in this system. A careful inspection of Figure 9b yields further insight into the nonmonotonic energy flow between the molecule and lattice. The beginning of the return of the Ar atom to the vicinity of its initial position *slightly precedes* in time the I_2 bond compression. The Ar atom is being pushed back toward the I_2 by an elastic response of the lattice, and it transmits this elastic energy back into the molecular vibration. The actual recombination of the molecule occurs during the second “attempt” at escape from the cage. During the second I–Ar cage interaction, over 500 cm^{-1} of energy is lost to the lattice; this is further reflected in the large-amplitude response of Ar (265) following this second collision shown in Figure 9b. A reexamination of Figure 5 at this point will reveal that the deexcitation of the I_2 below its dissociation threshold—the actual recombination event—*does not correlate with any notable feature in the observed signal*. This points out the danger of assigning features in ultrafast measurements to physically significant processes without the benefit of a detailed theoretical analysis.

We now extend our analysis of the same trajectory to examine the collective dynamics of the neighboring lattice atoms. In particular, we focus our attention on the six host Ar atoms forming the octahedral cage shown in Figure 8. These atoms are divided into two classes: the two axial atoms situated along the I–I bond, and the four equatorial atoms forming a “belt”

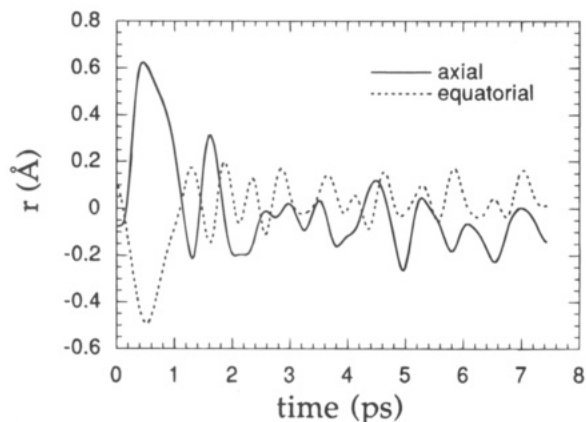


Figure 10. Time evolution of axial and equatorial modes, as defined in the text. Data are for the same trajectory as considered in Figure 9.

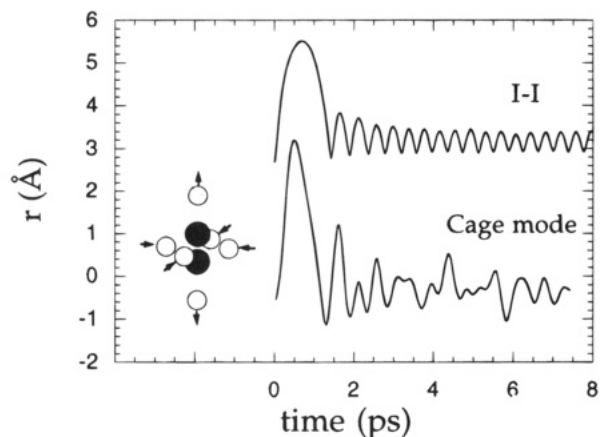


Figure 11. Representation of local cage dynamics by octahedral mode of E_g symmetry. See text for discussion.

around the molecule. We define two collective coordinates for the axial and an equatorial atoms:

$$r_{\text{axial}} = \frac{1}{2}(r_{236} + r_{265})$$

$$r_{\text{equatorial}} = \frac{1}{4}(r_{249} + r_{250} + r_{347} + r_{348}) \quad (8)$$

In Figure 10, the time dependence of these modes is shown. The initial photodissociation creates a large amplitude excitation in the axial mode, as expected from the single Ar atom dynamics of Figure 9b. The equatorial atoms are excited as well. However, their phase is shifted by 180° from the axial atoms: as the I–I bond lengthens, the equatorial belt “tightens” around the molecule. Figure 10 shows that this definite phase relation persists for at least two periods of their oscillation.

The dynamics of the axial and equatorial atoms in Figure 10 indicate that a well-defined collective mode of the cage is excited by the photodissociation of I_2 . In Figure 11, an alternative view of this collective motion is depicted, based on projecting the time-dependent positions of the Ar atoms onto one of normal modes of E_g symmetry of the octahedral point group (solid line). A sketch of the atomic displacements of this mode is shown as an inset. Also shown for comparison in Figure 11 is the I–I bond extension vs time. The cage dynamics are strongly driven by the I_2 photodissociation. At long times, the local excitation of the Ar cage is rapidly damped by coupling to the remainder of the lattice. However, as we noted above, the behavior of the system during the first 2 ps following the pump pulse and, in particular, the processes underlying the recombination event are not simple. I_2 bond re-formation is delayed by a flow of nearly 500 cm^{-1} back into the I_2 from the

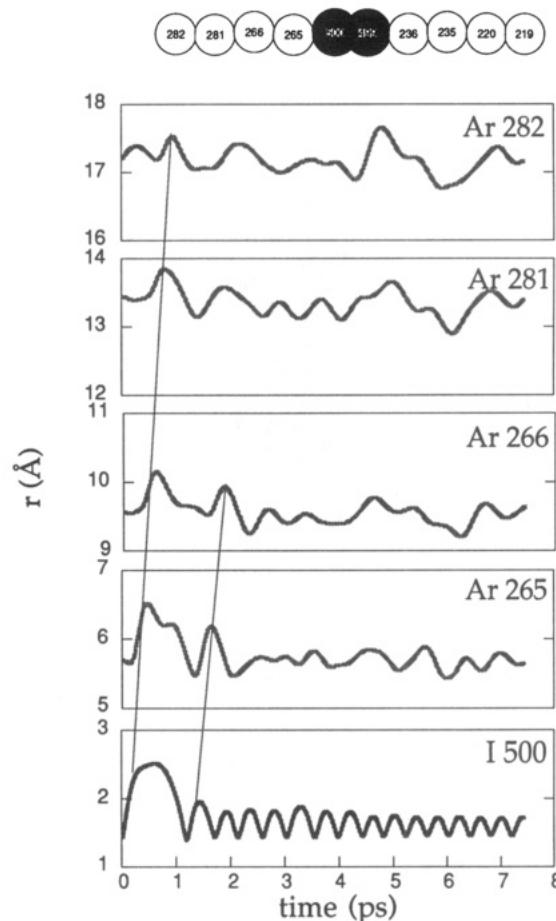


Figure 12. Time dependence of atomic positions along [111] axis vs time. See text for discussion.

lattice during the compression of the molecular bond following collision of the photofragments into the Ar cage. Figure 11 gives a particularly clear view of this elastic response of the lattice and its effect on the iodine impurity: the compression of the E_g mode following its first outer turning point occurs *more rapidly* than that of the I_2 . The I atoms are pushed inward by this mode, which is itself driven by the many-body elastic restoring force of the Ar lattice. This bath-induced acceleration of the I photofragments pumps in a significant amount of vibrational energy into the molecule, delaying recombination until this energy can be returned, later, to the lattice.

In Figure 12, we investigate the spatial transport of energy deposited by the photodissociation through the lattice. In particular, we examine the dynamics of the one-dimensional collinear chain of atoms along the [111] direction of the crystal. We consider the same 705 nm trajectory that we have been discussing throughout this section. The numbering of these atoms is indicated at the top of Figure 12. The data shown indicate the absolute positions, projected along the [111] direction, of one I atom and four consecutive Ar atoms; these atoms make up the left side of the accompanying diagram. The figure indicates that energy is rapidly transported in a quasi-one-dimensional manner along this chain of atoms in the form of a nanoscale shock wave.⁴⁴ The line indicates the approximate position of the propagating front of the first shock wave, created by the initial photodissociation. In addition, a secondary shock wave is indicated, which decays quickly due to the increased disorder of the perturbed lattice. This shock is created by the second I–Ar collision that, as discussed earlier, is responsible for the permanent recombination of this trajectory. In a recently reported theoretical study of the dynamics of shock waves in Ar lattices generated by photodissociation in a simple two

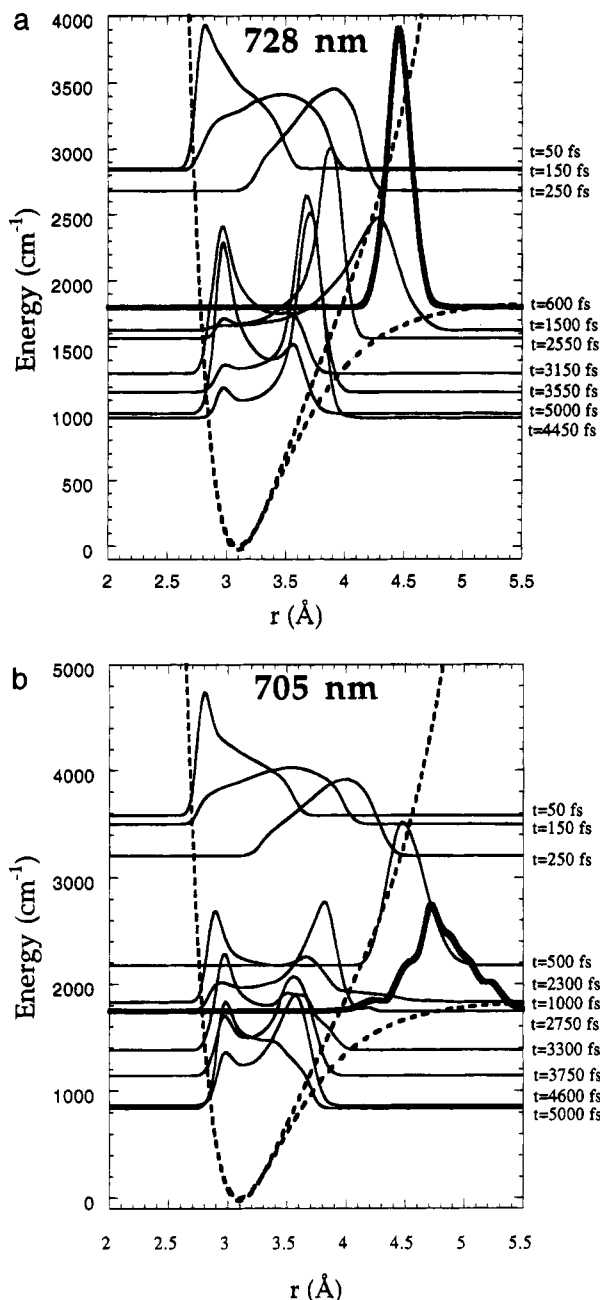


Figure 13. Classical wave-packet dynamics for (a) 728 nm pump excitation and (b) 705 nm excitation. See text for discussion.

dimensional model containing 2500 atoms,⁴⁴ it was found that energy transfer is highly localized in one dimension, in accord with the results of these full three-dimensional simulations.

(d) Origin of Vibrational Coherence. We now return our attention to the question of vibrational coherence in the photodissociation–recombination dynamics. The oscillations observed in the measured signals presented in Figures 2 and 5 are due to *spatial* coherence—defined here as the localization of the ensemble of trajectories, or quantum mechanically, the probability density $|\psi|^2$ —in configuration space. This is to be contrasted with coherence at the amplitude or phase level in quantum mechanics, such as a definite phase relation between vibrational wave functions on different electronic states. Our simulation results show that this spatial coherence can, at least for this system, be well-modeled classically.

The relation between the photodissociation and recombination processes and the resulting coherence is investigated in Figure 13, where the classical “wave packet” dynamics of the system, calculated by superimposing a swarm of Gaussians, each centered on a classical trajectory of the ensemble (see discussion

accompanying eq 4), is shown. A number of snapshots of the evolving I_2 coordinate probability distribution $\rho(R,t)$ are given; each snapshot has been further “blurred” by convoluting a family of instantaneous densities at different times with the pump-pulse temporal profile, so that the probability densities shown correspond to those actually created by the finite duration (100 fs) pump pulse. The baseline of each probability density corresponds to the average energy of the snapshot. In addition to the ensemble dynamics, the A state potential plus static cage contribution is shown. The mean time of each snapshot is given on the right side of the plot. Figure 13a shows the resulting evolution for an ensemble of trajectories generated by a 728 nm pump pulse, while Figure 13b shows the results for the higher energy 705 nm pulse.

We now examine some of the key aspects of the dynamics that can be discerned from examination of Figure 13a,b. Upon completion of the pump pulse, it is seen that a wavepacket spread over ~ 1 Å along the I–I coordinate is prepared. The wave packet immediately starts losing energy, due to the effective friction exerted on the molecule by the bath. It comes to a stop *beyond* the sudden wall, as a result of the elastic response of the cage to the photodissociation. The ensemble is completely caged at both energies, resulting in unit probability of recombination. Over a time scale of picoseconds, vibrational relaxation occurs, as depicted by the slow decrease of the energy baselines in Figure 13. The spatial localization of the ensemble persists at both energies until the end of the data shown (approximately $t = 5$ ps) and is responsible for the oscillations in the observable signals.

For the lower energy excitation of the 728 nm ensemble shown in Figure 13a, the collision of the evolving ensemble with the cage wall actually *focuses* the wave packet at the walls of the elastically deformed cage. This is an interesting example of system–bath interaction which actually *induces* vibrational coherence. Some focusing occurs in the higher energy case of 705 nm excitation, shown in Figure 13b; however, the packet is much more broken up by the caging, with a significant spread of trajectories out to relatively large I_2 distances. As the iodine bond is re-formed by recombination, the increased dispersion at the time of the cage collision is translated into a decrease in the spatial localization of the ensemble during the subsequent vibrational relaxation. Consequently, the depth of modulation of the observed signal is less in the 705 nm case than for the 728 nm measurement.

It is informative to compare the extent of coherence in Ar to that previously reported in Kr. In the latter case, both experiment and simulation show significantly reduced coherence under initial preparation conditions identical to those employed here. The equivalent representation of Figure 13 indicated that, for Kr, the dispersion in recombination times significantly exceeds the bound I_2 vibrational period, leading to a marked reduction in the spatial coherence in the oscillating flux. This behavior is the result of important differences in the dynamics of the collision of photofragments with the cage, which is clearly demonstrated by the phase portrait plots shown in Figure 14. Here, a representative set of trajectories are collected for the first 2 ps of time evolution and displayed on the position–momentum phase portrait of the I_2 vibrational degree of freedom. The collision with the cage, which occurs at the right-outer turning point of the plots, is dramatically different in the Ar and Kr cases. In Ar, the trajectories are accelerated by the recoil force of the elastic cage, and the inward moving (negative momentum) part of the phase curve is approximately the reflection of the outgoing (positive momentum) branch. Note

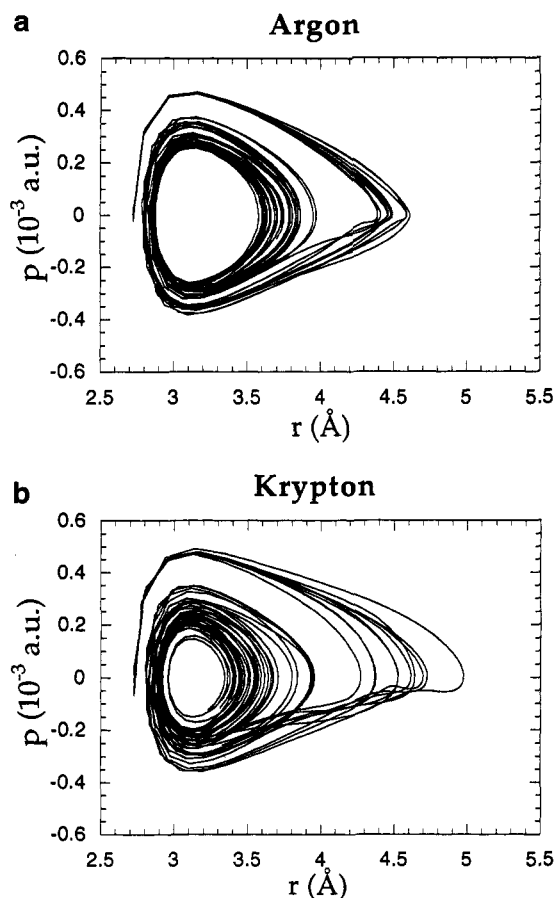


Figure 14. I_2 phase portrait representation of the early-time photodissociation–recombination dynamics. (a) argon, (b) krypton. See text for discussion.

that a perfectly symmetric response (i.e., a phase plot that is invariant under $R \rightarrow -R$) is the limiting behavior of nondissipative dynamics of I_2 in a completely elastic cage. In Kr, after deceleration, the trajectories slowly return with nearly zero lattice restoring force. The asymmetry of the phase plot for the first cycle in this case is representative of a dissipative cage deformation, rather than an elastic recoil. As a result, I_2 trajectories in Ar possess a well-defined oscillator phase, representative of coherent vibrational energy relaxation, while in Kr there is a much larger dispersion in the oscillator phase. These significant differences arise from the kinematics of the caging. Due to the larger mass asymmetry in the case of Ar, the I atoms are stopped only after driving the cage far enough out to elicit an elastic recoil from the rest of the lattice. In Kr, due to the smaller mass asymmetry, the first binary collision has a significantly higher “stopping power” for the I photo-fragments. In addition, it seems that the relative sizes of the isolation sites also play a role in producing the observed differences. The larger cage size in Kr is responsible for the longer bond extension to the first turning point in Figure 14.

When the quantitative level of coherence observed in the signal is considered (see Figure 5a), it is apparent that the simulations exhibit substantially more coherence than observed in the experiment at 705 nm. For lower energies and for I_2 in Kr, the agreement is much closer. There are a number of possible origins for this, including dispersion of the resonant configurations for probe absorption, due to the *dynamic* nature of the ion-pair D state solvation, which is not being modeled in the simulations, which are based on a *sharp* position for the resonance windows. In general, any such mechanism that is omitted from the calculations will act to spuriously enhance theoretical coherence in the synthesized signal.

VII. Concluding Remarks

In this paper, we have described real-time investigations of the photodissociation and recombination of I_2 in an Ar lattice. The results presented demonstrate the value of ultrafast pump–probe experiments for studying the complex many-body dynamics of condensed media driven far from equilibrium. In contrast with frequency domain experiments, detailed information about the dynamics of the coupled molecule-bath system can be obtained in real time, providing a view of molecular processes on chemically relevant time and length scales. The information contained in the observables is quite rich. However, the underlying dynamics of the system involve many coupled degrees of freedom behaving in a highly nonlinear manner, making it difficult to extract insight from the experimental data alone. To meet this challenge, we have closely coupled our experimental studies with theoretical modeling via molecular dynamics simulations and have iterated between the two complimentary tools of ultrafast spectroscopy and large-scale computer simulation in developing our microscopic picture of the photodissociation, caging, and geminate recombination of I_2 in rare gas solids.

We reported pump–probe signals for the system at several pump wavelengths and presented time-resolved photoselection measurements which indicate that the observed dynamics proceed on a single electronic surface. For all cases considered, substantial coherence was observed in the ultrafast vibrational dynamics of the system, as reflected in pronounced oscillations superimposed on the overall envelope of the experimental response. A detailed comparison of the experimental results obtained at a pump wavelength of 705 nm and simulated signals calculated using molecular dynamics and the classical Franck–Condon principle were presented. Excellent correlation between the salient features in the signals was obtained, giving confidence that the dynamics of the photodissociation and recombination are being accurately modeled by the simulations. We then went on to examine in detail the atomistic dynamics of the system—information that is not accessible experimentally.

A number of notable features of the microscopic dynamics and their relation to experimental observables were revealed by our analysis of the trajectory data. Of particular interest was the spatial and energetic aspects of the I_2 caging and the recombination. For the 705 nm excitation, we saw that the I–I bond returns spatially to the initial configuration space region at the inner turning point of the A state after approximately one picosecond. Energetically, however, the I_2 bond has not yet reformed, due to the flow of several hundred wavenumbers of energy from the lattice to the molecule during the bond compression immediately following the first attempt at cage escape by the photofragments. This energy, which was initially deposited into the lattice by the I atoms, has been stored in the collective modes of the elastic cage response without immediate dissipation into lattice thermal motion. A significant fraction remains available to flow back into the I_2 during the I–I bond compression, leading to a molecule which is still energetic enough to dissociate. In this sense, recombination of the molecule has not yet occurred. Only on the *second* I–I bond extension does the energy of the molecule drop below its dissociation threshold.

The results presented here provide a detailed view of the coupled system-bath dynamics occurring during the first few picoseconds following the creation of a highly nonequilibrium vibrational excitation on the excited (A) electronic state of the system. Analysis of the simulated trajectories revealed highly specific pathways of energy flow out of—and back into—the I_2 chromophore. In addition, persistent and coherent excitations of nonlinear modes of the lattice, such as the strongly driven

E_g symmetry cage deformation mode and the localized shock waves, were observed. These phenomena illustrate the strongly nonequilibrium nature of the bath on the time scale of 1–2 ps. The standard formal theories of condensed phase reactions, such as Kramers theory¹ and Grote–Hynes theory¹, in addition to stochastic computational methods such as the generalized Langevin equation approach,¹ rely on an assumption of a harmonic bath that is characterized by a well-defined temperature. These assumptions are clearly breaking down under the present conditions. Our increasing ability to view the dynamics of many-body “bath” degrees of freedom using ultrafast spectroscopy and to analyze complex systems using computer simulation promises to yield deeper insight into many-body dynamics beyond these simple approximations.

Acknowledgment. V.A.A. acknowledges support by the AFOSR, under a University Research Initiative grant F49620-1-0251. C.C.M. acknowledges support from the National Science Foundation and the Office of Naval Research. The UCI Office of Academic Computing and the Pittsburgh Supercomputing Center provided the computer resources used to perform the simulations reported here.

References and Notes

- (1) See, for example: Hynes, J. T. In *Theory of Chemical Reaction Dynamics*, Baer, M., Ed.; CRC Press: Boca Raton, FL, 1985. Hynes, J. T. *Annu. Rev. Phys. Chem.* **1985**, *36*, 573. Harris, A. L.; Brown, J. K.; Harris, C. B. *Annu. Rev. Phys. Chem.* **1988**, *39*, 341. Whitnell, R. M.; Wilson, K. R. In *Reviews of Computational Chemistry*; Vol. IV, Lipkowitz, K. B., Boyd, D. B., Eds.; VCH: New York, 1994; pp 67–184.
- (2) Franck, J.; Rabinowitch, E. *Trans. Faraday Soc.* **1934**, *30*, 120. Rabinowitch, E.; Wood, W. C. *Ibid.* **1936**, *32*, 547; **1936**, *32*, 1381.
- (3) Noyes, R. M. *Prog. React. Kinet.* **1961**, *1*, 130.
- (4) Luther, K.; Troe, J. *J. Chem. Phys. Lett.* **1984**, *24*, 85. Otto, B.; Schroeder, J.; Troe, J. *J. Chem. Phys.* **1984**, *81*, 202.
- (5) Chergui, M.; Schwentner, N. *Trends Chem. Phys.* **1992**, *2*, 89.
- (6) Chuang, T. J.; Hoffman, G. W.; Eisenthal, K. B. *Chem. Phys. Lett.* **1974**, *25*, 201.
- (7) Langhoff, C. A.; Moore, B.; DeMeuse, M. *J. Am. Chem. Soc.* **1982**, *104*, 3576.
- (8) Kelly, D. F.; Rentzepis, P. M. *Chem. Phys. Lett.* **1982**, *85*, 85.
- (9) Bado, P.; Dupuy, C.; Magde, D.; Wilson, K. R.; Malley, M. M. *J. Chem. Phys.* **1984**, *80*, 5531.
- (10) Kelley, D. F.; Abul-Haj, N. A.; Jang, D. J. *J. Chem. Phys.* **1984**, *80*, 4105. Abul-Haj, N. A.; Kelley, D. F. *Chem. Phys. Lett.* **1985**, *119*, 182. Abul-Haj, N. A.; Kelley, D. F. *J. Chem. Phys.* **1986**, *84*, 1335.
- (11) Harris, A. L.; Berg, M.; Harris, C. B. *J. Chem. Phys.* **1986**, *84*, 788. Smith, D. E.; Harris, C. B. *J. Chem. Phys.* **1987**, *87*, 2709. Paige, M. E.; Harris, C. B. *Chem. Phys.* **1990**, *149*, 37.
- (12) Schwartz, B. J.; King, J. C.; Zhang, J. Z.; Harris, C. B. *Chem. Phys. Lett.* **1993**, *203*, 503.
- (13) Lingle, R.; Xu, X.; Yu, S.-C.; Zhu, H.; Hopkins, J. B. *J. Chem. Phys.* **1990**, *93*, 5667. Xu, X.; Yu, S.-S.; Lingle, R.; Zhu, H.; Hopkins, J. B. *J. Chem. Phys.* **1991**, *95*, 2445.
- (14) Scherer, N. F.; Ziegler, L. D.; Fleming, G. R. *J. Chem. Phys.* **1992**, *96*, 5544. Scherer, N. F.; Jonas, D. M.; Fleming, G. R. *J. Chem. Phys.* **1993**, *99*, 153.
- (15) Johnson, A. E.; Levinger, N. E.; Barbara, P. F. *J. Phys. Chem.* **1992**, *96*, 7841.
- (16) Banin, U.; Waldman, A.; Ruhman, S. *J. Chem. Phys.* **1992**, *96*, 2416.
- (17) Zadoyan, R.; Li, Z.; Ashjian, P.; Martens, C. C.; Apkarian, V. A. *Chem. Phys. Lett.* **1994**, *218*, 504.
- (18) Zadoyan, R.; Li, Z.; Martens, C. C.; Apkarian, V. A. *Proc. SPIE* **1994**, *2124*, 233.

- (19) Zadoyan, R.; Li, Z.; Martens, C. C.; Apkarian, V. A. In *Ultrafast Phenomena IX*; Barbara, P. F., Knox, W. H., Mourou, G. A., Zewail, A. H., Eds.; Springer Series in Chemical Physics Vol. 60; Springer: New York, 1994; p 79.
- (20) Zadoyan, R.; Li, Z.; Martens, C. C.; Apkarian, V. A. *J. Chem. Phys.* **1994**, *101*, 6648.
- (21) Brown, J. K.; Harris, C. B.; Tully, J. C. *J. Chem. Phys.* **1988**, *89*, 6687.
- (22) Benjamin, I.; Wilson, K. R. *J. Chem. Phys.* **1989**, *90*, 4176.
- (23) Benjamin, I.; Banin, U.; Ruhman, S. *J. Chem. Phys.* **1993**, *98*, 8337.
- (24) Saenger, K. L.; McClelland, G. M.; Herschbach, D. R. *J. Phys. Chem.* **1981**, *85*, 3333.
- (25) Valentini, J. J.; Cross, J. B. *J. Chem. Phys.* **1982**, *77*, 572.
- (26) NoorBatcha, I.; Raff, L. M.; Thompson, D. L. *J. Chem. Phys.* **1984**, *81*, 12.
- (27) Amar, F. G.; Berne, B. J. *J. Phys. Chem.* **1984**, *88*, 6720.
- (28) Alimi, R.; Brokman, A.; Gerber, R. B. In *Stochasticity and Intramolecular Redistribution of Energy*; Lefebvre, R., Mukamel, S., Eds.; Reidel: Dordrecht, 1987; p 233.
- (29) Beswick, J. A.; Monot, R.; Phillipoz, J.-M.; van den Bergh, H. *J. Chem. Phys.* **1987**, *88*, 3965.
- (30) Phillipoz, J. M.; Melinon, P.; Monot, R.; van den Bergh, H. *Chem. Phys. Lett.* **1987**, *138*, 579.
- (31) Burke, M. L.; Klemperer, W. *J. Chem. Phys.* **1993**, *98*, 1797.
- (32) Alimi, R.; Gerber, R. B. *Phys. Rev. Lett.* **1990**, *64*, 1453.
- (33) Fei, S.; Zheng, X.; Heaven, M.; Tellinghuisen, J. *J. Chem. Phys.* **1992**, *97*, 6057.
- (34) Ray, D.; Levinger, N. E.; Papanikolas, J. M.; Lineberger, W. C. *J. Chem. Phys.* **1989**, *91*, 6533. Papanikolas, J. M.; Gord, J. R.; Levinger, N. E.; Ray, D.; Vorsa, V.; Lineberger, W. C. *J. Phys. Chem.* **1991**, *95*, 8028. Papanikolas, J. M.; Vorsa, V.; Nadal, M. E.; Campagnolo, P. J.; Gord, J. R.; Lineberger, W. C. *J. Chem. Phys.* **1992**, *97*, 7002. Papanikolas, J. M.; Vorsa, V.; Nadal, M. E.; Campagnola, P. J.; Buchenau, H. K.; Lineberger, W. C. *J. Chem. Phys.* **1993**, *99*, 8733.
- (35) Garcia-Vela, A.; Gerber, R. B.; Valentini, J. J. *J. Chem. Phys.* **1992**, *97*, 3297.
- (36) Potter, E. D.; Liu, Q.; Zewail, A. H. *Chem. Phys. Lett.* **1992**, *200*, 605. Liu, Q.; Wang, J. K.; Zewail, A. H. *Nature*, **1993**, *364*, 427.
- (37) Finney, L. M.; Martens, C. C. *J. Phys. Chem.* **1992**, *96*, 10626; **1993**, *97*, 13477.
- (38) Myers, A. B. *J. Opt. Soc. Am. B (Opt. Phys.)* **1990**, *7*, 1665.
- (39) Beeken, P. B.; Mandich, M.; Flynn, G. W. *J. Chem. Phys.* **1982**, *76*, 5995. Mandich, M.; Beeken, P. B.; Flynn, G. W. *J. Chem. Phys.* **1982**, *77*, 702. Beeken, P. B.; Hanson, E. A.; Flynn, G. W. *J. Chem. Phys.* **1983**, *78*, 5892.
- (40) Macler, M.; Nicolai, J.-P.; Heaven, M. *J. Chem. Phys.* **1989**, *91*, 674.
- (41) Kono, H.; Lin, S. H. *J. Chem. Phys.* **1986**, *84*, 1071.
- (42) Howard, W. F.; Andrews, L. *J. Raman Spectrosc.* **1974**, *2*, 497. Grzybowski, J. M.; Andrews, L. *J. Raman Spectrosc.* **1975**, *4*, 99.
- (43) (a) Xu, J.; Schwentner, N.; Chergui, M. *J. Chem. Phys.*, in press. (b) Sension, R. J.; Strauss, H. L. *J. Chem. Phys.* **1986**, *85*, 3791. Sension, R. J.; Kobayashi, T.; Stauss, H. L. *J. Chem. Phys.* **1987**, *87*, 6221, 6233.
- (44) Borrmann, A.; Martens, C. C. *J. Chem. Phys.* **1995**, *102*, 1905.
- (45) Tellinghuisen, J. *J. Can. Phys.* **1984**, *62*, 1933.
- (46) Macler, M.; Heaven, M. *Chem. Phys.* **1991**, *151*, 219.
- (47) Franck, J. *Trans. Faraday Soc.* **1925**, *21*, 536.
- (48) Pugliano, N.; Palit, D. K.; Szarka, A. Z.; Hochstrasser, R. M. *J. Chem. Phys.* **1993**, *99*, 7273.
- (49) Tellinghuisen, J. *J. Chem. Phys.* **1985**, *82*, 4012.
- (50) Böbling, R.; Langen, J.; Schurath, U. *Chem. Phys.* **1989**, *130*, 419.
- (51) Albrecht, A. C. *J. Mol. Spectrosc.* **1961**, *6*, 84.
- (52) Klinger, D. S.; Lewis, J. W.; Randall, C. E. *Polarized Light in Optics and Spectroscopy*; Academic Press: New York, 1990; Chapter 7.
- (53) Fincham, D.; Heyes, D. M. *Adv. Chem. Phys.* **1985**, *63*, 493. *Simulation of Liquids and Solids*; Ciccotti, G., Frenkel, D., McDonald, I. R., Eds.; North-Holland: New York, 1987. Allen, M. P.; Tildesley, D. J. *Computer Simulation of Liquids*; Clarendon: Oxford, 1987. Hockney, R. W.; Eastwood, J. W. *Computer Simulation Using Particles*; Adam Hilger: Philadelphia, 1988.
- (54) Scoles, G. *Ann. Rev. Phys. Chem.* **1980**, *31*, 81.
- (55) Wigner, E. P. *Phys. Rev.* **1932**, *40*, 749.
- (56) Bergsma, J. P.; Berens, P. H.; Wilson, K. R.; Fredkin, D. F.; Heller, E. *J. Phys. Chem.* **1984**, *88*, 612.
- (57) See, for example: Yan, Y. J.; Mukamel, S. *Phys. Rev. A* **1990**, *41*, 6485.